Journal of Power Sources 623 (2024) 235401

Contents lists available at ScienceDirect

Journal of Power Sources

journal homepage: www.elsevier.com/locate/jpowsour

Operando pH measurements revealing the promoted Zn^{2+} intercalation kinetics of pre-intercalated V_2O_5 cathode in aqueous zinc metal batteries

Xu Liu [a,b], Xu Dong [a,b,**], Stefano Passerini [a,b,c,*]

[a] Helmholtz Institute Ulm (HIU) Electrochemical Energy Storage, Helmholtzstrasse 11, 89081, Germany
[b] Karlsruhe Institute of Technology (KIT), PO Box 3640, D-76021, Karlsruhe, Germany
[c] Austrian Institute of Technology (AIT), Center for Transport Technologies, Giefinggasse 4, 1020, Wien, Austria

HIGHLIGHTS

- Zn^{2+} pre-intercalated V_2O_5 synthesis via microwave reaction.
- Effect of pre-intercalated Zn^{2+} to the specific capacity of V_2O_5.
- *Operando* pH measurements as a tool to reveal AZMB intercalation mechanism.
- H^+ and Zn^{2+} de-/intercalation in Zn^{2+} pre-intercalated V_2O_5.

GRAPHICAL ABSTRACT

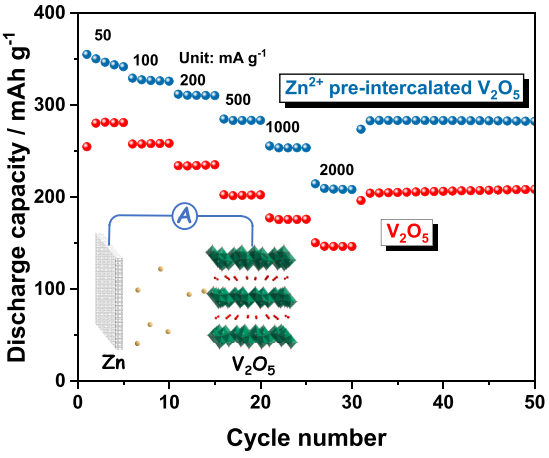

ARTICLE INFO

Keywords:
Bilayered V_2O_5
Intercalation mechanism
Aqueous zinc metal battery
Operando pH measurement
Intercalation kinetics

ABSTRACT

Pre-intercalating metallic cations into the interlayer spacing of vanadium oxides is considered as a promising strategy to promote the de-/intercalation kinetics in Zn^{2+}-based aqueous electrolytes for high-performance aqueous zinc metal batteries. However, the respective role of H^+ and Zn^{2+} de-/intercalation in the promoted electrochemical performance is not well understood due to the lack of suitable characterization methods. Herein, Zn^{2+} pre-intercalated and neat bilayered V_2O_5 prepared via a highly efficient microwave-assisted hydrothermal method were selected as model compounds to study the effect of the pre-intercalated ions through combining *operando* electrolyte pH measurement with conventional structural and electrochemical characterization. The Zn^{2+} pre-intercalated V_2O_5 exhibits higher specific capacity than the neat V_2O_5 in a wide current rate, increasing from 281 to 355 mAh g^{-1} at 50 mA g^{-1}, and capacity retention of 84 % after 500 cycles at 2000 mA g^{-1}. The mechanism study demonstrates that the de-/intercalation of H^+ and Zn^{2+} mainly occurs in the high voltage and low voltage regions, respectively. Although the intercalation kinetics of both H^+ and Zn^{2+} is promoted due to the

* Corresponding author. Helmholtz Institute Ulm (HIU) Electrochemical Energy Storage, Helmholtzstrasse 11, 89081, Germany.
** Corresponding author. Helmholtz Institute Ulm (HIU) Electrochemical Energy Storage, Helmholtzstrasse 11, 89081, Germany.
E-mail addresses: xu.dong@kit.edu (X. Dong), stefano.passerini@kit.edu (S. Passerini).

https://doi.org/10.1016/j.jpowsour.2024.235401
Received 13 July 2024; Received in revised form 1 September 2024; Accepted 3 September 2024
Available online 8 September 2024

enlarged interlayer distance from 11.6 to 13.4 Å, the Zn^{2+} intercalation as the step limiting the specific capacity contributes more to the capacity enhancement.

1. Introduction

Lithium-ion batteries, as the state-of-the-art battery technology, dominate the market of portable electronics and is now promoting the deployment of electric vehicles and stationary energy storage [1,2]. At the same time, their safety risk originating from the use of highly flammable organic liquid electrolytes stimulates the investigation of complementary batteries employing safer aqueous electrolytes. However, the inferior electrochemical stability window of aqueous electrolytes with respect to the nonaqueous electrolytes lowers the energy density of aqueous batteries [3]. In this context, zinc metal with a high specific capacity of 820 mAh g^{-1} and 5855 mAh cm^{-3} is an appealing anode material to improve the battery energy density. Particularly, high reversibility of zinc stripping/plating with Coulombic efficiency higher than 99.7 % has been reported [4,5], thanks to the rapid development of novel anode and electrolytes [6–8], promising the feasible development of long-lifespan aqueous zinc metal batteries (AZMBs).

Cathode materials are also an important component determining the energy density, rate capability, and cycling stability of AZMBs. Up to now, there has been several types of cathode materials for AZMBs, e.g., vanadium oxides [9], manganese oxides [10], Prussian blue analogues [11], polyanionic compounds [12], iodine [13], and chalcogens [14]. Among them, vanadium oxides exhibiting high specific capacity, rate capability, and cyclability receive numerous attentions. Their chemical and structural tunability leads to the emergence of different vanadium oxide-based cathode materials [15], and it has been generally realized that pre-intercalating metallic ions into the interlayer spacing of vanadium oxides can promote their de-/intercalation kinetics in Zn^{2+}-based aqueous electrolytes due to the enlarged interlayer distance [16–19]. Nonetheless, it should be noticed that both H^+ and Zn^{2+} existing in the electrolytes can be intercalated into vanadium oxides [20,21]. The respective role of H^+ and Zn^{2+} de-/intercalation in the promoted electrochemical performance is not well understood, resulting from that the conventional structural and elemental characterization methods not being adequate to separate the roles of H^+ and Zn^{2+} intercalations in Zn^{2+}-based aqueous electrolytes [22]. First, both H^+ and Zn^{2+} are intercalated into layered vanadium oxides via solid solution processes [22], which eliminates the support of structural characterization methods supplying interlayer distances, e.g., X-ray and electron diffraction, as well as high-resolution transmission electron microscopy. Second, the intercalation of H^+ into vanadium oxides is usually accompanied with the formation of basic zinc salts [20], e.g., $Zn_4SO_4(OH)_6$, in aqueous $ZnSO_4$ electrolytes [21]. These by-products contain zinc, but are not related to the intercalation of Zn^{2+}. Therefore, the elemental characterization methods are not feasible to identify Zn^{2+} intercalation, e.g., X-ray photoelectron spectroscopy and energy dispersive spectrometry (EDS). In our previous work, an *operando* electrolyte pH measurement was developed, sensitively monitoring the pH variation of the electrolyte in close proximity to the working electrode in a designed cell with a low amount electrolyte (only 100 μL per cell) [22]. This *operando* technique revealed the combined H^+/Zn^{2+} intercalation chemistry of vanadium oxide in AZMBs, which is promising to promote the understanding of the enhanced electrochemical performance of pre-intercalated vanadium oxides.

Herein, Zn^{2+} pre-intercalated bilayered V_2O_5 (ZVO) and neat bilayered V_2O_5 (VO) prepared via a highly efficient microwave-assisted hydrothermal method are selected as model compounds to study the effect of Zn-ion pre-intercalation in the cathode material on the electrochemical performance of AZMBs with *operando* pH measurements, XRD, and electrochemical tests. The pre-intercalated Zn^{2+} increases the specific capacity of V_2O_5, e.g., from 281 to 355 mAh g^{-1} at 50 mA g^{-1}. The pre-intercalation increases the interlayer distance from 11.6 to 13.4 Å, facilitating the electrochemical de-/intercalation of both H^+ and Zn^{2+}, but the enhanced specific capacity mainly originates from the de-/intercalation of Zn^{2+}.

2. Results and discussion

2.1. Physical characterization

ZVO and VO were prepared via a microwave-assisted hydrothermal method. Making use of the dielectric heating mode, these materials were obtained in 30 min at 180 °C, which is much faster than traditional sol-gel methods requiring tens of hours for the reactions [23,24].

Fig. 1a shows the powder XRD patterns of the obtained materials. For VO, the position and relative intensity of the diffraction reflections match well with the standard Bragg positions of bilayered $V_2O_5{\cdot}H_2O$ (ICSD: 94905). Its crystal structure model projected along [010] direction is shown in Fig. 1b. The polyhedrons with V^{5+} and O^{2-} as the central and ligand atoms, respectively, link to form V-O layers. The oxygens in the interlayers represent the oxygen atoms of water. The XRD reflection located at 7.59° results from the (001) crystal plane, of which the corresponding interplanar spacing ($d_{(001)}$, 11.6 Å) reflects the space between the adjacent V-O slabs, as illustrated in Fig. 1b. With Zn^{2+} intercalated, the diffraction reflections of (001), (003), (004), and (005) shift to lower angles, indicating the increased interlayer spacing. This behavior is identical to the previous literatures [16,19,25]. Based on their angles, the interplanar spacing of (001) was calculated to be 13.4 Å. The position of the pre-intercalated Zn^{2+} in the structure has been previously investigated via X-ray adsorption spectroscopy technique. It is demonstrated that Zn^{2+} are 4-fold coordinated by almost coplanar oxygens in $V_2O_5{\cdot}H_2O$ [26–28]. Since the guest ions, e.g., H^+ and Zn^{2+}, are intercalated into the space between the V-O slabs during the discharge, the increased $d_{(001)}$ value due to the pre-intercalated Zn^{2+} is expected to promote the electrochemical performance.

Thermogravimetric analysis (TGA) of the samples was carried out under N_2 atmosphere with a heating rate of 5 °C min^{-1}. As shown in Fig. 1c, the weight loss corresponds to the elimination of water from the materials, which can be divided into three processes at different temperature ranges. For VO, the weight loss before 100 °C originates from the desorption of free water on the particle surface [29]. The weight loss at higher temperatures is associated with the water molecules in the interlayers. Among them, the water molecules relatively weakly bounded escape between 100 and 230 °C, while the more stably bounded water molecules are removed at higher temperatures, e.g., 230–300 °C [29]. The TGA curve of ZVO can also be divided to these three processes, but all of them occurs at higher temperatures, which implies a better thermal stability of the pre-intercalated sample. Compared with VO, the pre-intercalated sample exhibits generally fewer water contents but more absorbed water. Therefore, the water molecules in the interlayer of ZVO is lower than that in VO, which also demonstrates that the high $d_{(001)}$ value of ZVO is caused by the pre-intercalated Zn^{2+} rather than the water molecules in the interlayer.

In Fig. 1d, the N_2 adsorption-desorption isotherm curves of the powder samples show typical feature of the H3 hysteresis, indicating the slit-shaped pores associated with the aggregates of plate-like particles [30]. The specific surface area of VO and ZVO was calculated to be 3.5 and 4 m^2 g^{-1}, respectively, via Brunauer-Emmett-Teller (BET) model.

The morphology of the samples was observed via scanning electron microscope (SEM). A bulky VO particle with a size larger than 100 μm is observed in Fig. 2a. The top of the particle is quite dense and flat, while the SEM image of its edge (Fig. 2b) reveals that this is a secondary

particle consisting of primary V_2O_5 layers. This fits well with the H3 hysteresis of its N_2 adsorption-desorption isotherm curve (Fig. 1d). Fig. 2c and d display the SEM images of ZVO. Compared with VO, the pre-intercalated sample shows smaller and more porous primary particles consisting of thin flakes. Despite the different morphologies of VO and ZVO, it should be noted that the specific surface area of the two materials is very similar. Since specific surface area determines the sites for electrochemical reaction, the promotion of the electrochemical performance associated with the morphology is expected to be very limited. Fig. 2e shows the EDS elemental mapping of the ZVO particles. The distribution of oxygen, vanadium, and zinc was found to be uniform and in good agreement with the secondary electron image. The Zn and V content in ZVO measured by Inductively Coupled Plasma - Optical Emission Spectroscopy (ICP-OES) were 4.73 wt% and 45.6 wt%, respectively, yielding a Zn/V molar ratio of 0.162:2.

2.2. Electrochemical performance

The electrochemical properties of the prepared materials were evaluated with coin cells employing a 3 m aqueous solution of zinc triflate ($Zn(OTF)_2$) as the electrolyte and zinc metal foil as the anode. The mass loading of the active material in the cathode was about 3 mg cm^{-2}.

Fig. 3a displays the cyclic voltammetry (CV) profile obtained at a scanning rate of 0.1 mV s^{-1}. Both the profiles show two pairs of broad redox peaks, of which the trough between the peaks in the anodic and cathodic scans is located around 0.75 V and around 0.9 V, respectively. This indicates the presence of multistep intercalation chemistry in the electrode materials. Compared with that for VO, the profile for ZVO generally exhibits larger area, demonstrating its higher electrochemical activity. Moreover, this phenomenon is more pronounced for the redox peaks at the lower voltage region, which implies that the low-voltage redox reaction receives stronger promotion effect from the Zn^{2+} pre-intercalated into the interlayer than the high-voltage one.

The specific capacity was further evaluated via galvanostatic dis-/charge. Fig. 3b displays the typical dis-/charge profiles obtained at 50 mA g^{-1}, and the specific discharge capacity at various current rates are summarized in Fig. 3c. The specific discharge capacity of VO at 50, 500, and 2000 mA g^{-1} was 281, 202, and 146 mAh g^{-1}, respectively. For ZVO at the same specific current rates, the specific discharge capacity was 355, 283, and 208 mAh g^{-1}, respectively. These results demonstrate the promotion effect of the Zn^{2+} pre-intercalation on the specific capacity. The cycling stability was evaluated at 500 mA g^{-1}. As displayed in Fig. 3d, both two materials exhibited stable cycling without significant capacity degradation in 100 cycles. The cell employing ZVO as the cathode material was further evaluated at 2000 mA g^{-1}. After 500 cycles, 84 % of the initial discharge capacity was retained, demonstrating its good cyclability as the cathode for AZMBs. The evolution of areal capacity upon cycling is supplied in Fig. S2. These electrochemical results reveal that pre-intercalating Zn^{2+} into the bilayered V_2O_5 can promote the specific capacity without obviously affecting its cyclability, which is identical to the previously reported pre-intercalated V_2O_5.

2.3. Mechanism study

Ex-situ XRD of VO and ZVO in the initial discharge and charge cycle was conducted and the collected XRD patterns are shown in Fig. 4a and b, respectively. In general, three features are observed from the diffraction patterns upon the first cycle. The first one is the reversible shift of V_2O_5 (001) reflection, which indicates the reversible change of the interlayer distance and the de-/intercalation of guest ions in the electrolyte upon the electrochemical reaction. For VO, the (001)

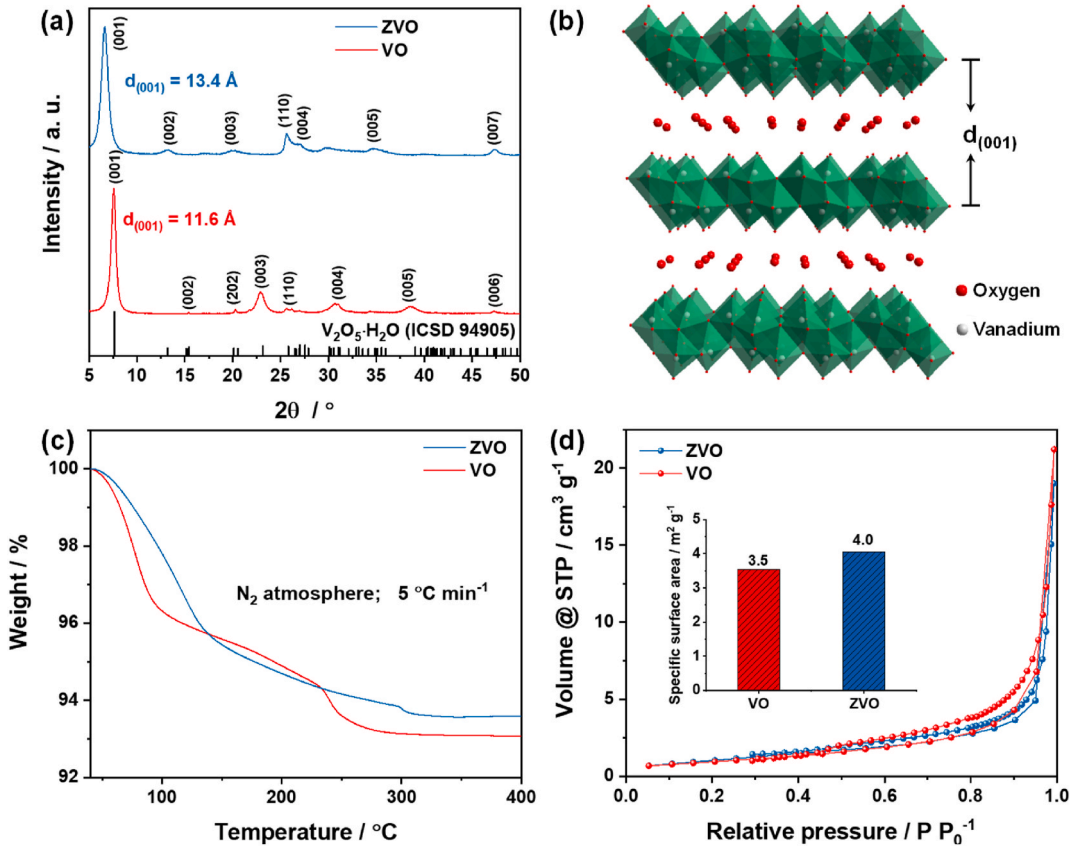

Fig. 1. Physical characterization of VO and ZVO. (a) XRD patterns. (b) The crystal structure model projected along [010]. (c) TGA curves obtained under N_2 atmosphere at a heating rate of 5 °C min^{-1}. (d) N_2 adsorption-desorption isotherm curves. The inset is the calculated BET specific surface area.

reflection gradually shifts to higher 2θ during the discharge, which indicates a decreasing interlayer distance when H^+ and/or Zn^{2+} are intercalated. This behavior can be attributed to the electrostatic force effect, i.e., the attracting force between the intercalated positively charged ions and the adjacent negatively charged V-O slabs, decreasing the interlayer distance [31]. The (001) reflection of ZVO shifts to lower 2θ during charge indicating for an increased interlayer spacing. This can be attributed to the volume effect of the intercalated guest ions. The opposite behavior observed from the two materials can be attributed to the different amount of the ions intercalated into the interlayer. The higher amount of the guest ions intercalated into ZVO makes the volume effect more pronounced than the electrostatic force. In fact, it has been reported that the interlayer distance of bilayered V_2O_5 is initially decreasing due to the electrostatic force effect and then increasing owing to more pronounced volume effect upon cation intercalation [32]. This effect correlates well with the highest specific capacity of ZVO. Since both H^+ and Zn^{2+} can be reversibly intercalated into the V_2O_5 interlayer, the observed shift of (001) reflection, unfortunately, cannot discriminate the intercalated ion.

The second feature occurs in the low voltage range (<0.8 V), where a few reflections located at 6.55°, 13.10°, and 19.70° appear upon discharge and disappear upon charge, corresponding to the formation of a layered compound with an interlayer distance of 13.5 Å. Previous literatures have proved that this new phase is a vanadium-free basic zinc salt ($Zn_x(OTF)_y(OH)_z$) generated from the intercalation of H^+ into V_2O_5 as described with the following chemical reactions [20,22]:

$$H_2O \leftrightarrow H^+ + OH^-$$

$$V_2O_5 + zH^+ + ze^- \rightarrow H_ZV_2O_5$$

$$xZn^{2+} + yOTF^- + zOH^- \rightarrow Zn_x(OTF)_y(OH)_z$$

The reversible formation of $Zn_x(OTF)_y(OH)_z$ indicates the occurrence of H^+ de-/intercalation. However, this compound contains zinc, but is not relevant to Zn^{2+} intercalation, making unfeasible the use of elemental analysis to discriminate the intercalation of H^+ or Zn^{2+}.

The third feature is the presence of $Zn_3(OH)_2V_2O_7{\cdot}2H_2O$ at high voltage range (≥1.2V), which is associated with the electrochemical anodic deposition of vanadium species previously dissolved in the electrolyte [33].

Overall, the analysis of the *ex-situ* XRD results evidences H^+ and/or Zn^{2+} intercalation into the cathode material, but does not allow to discriminate the role of H^+ and Zn^{2+} in the enhanced electrochemical performance. The previously designed *operando* pH measurement was then conducted on AZMBs employing VO and ZVO cathodes [22]. The configuration of the cell is displayed in Fig. S3. The pH value of the electrolyte in close proximity to the working electrode during the initial discharge and charge at 50 mA g^{-1} is displayed in Fig. 4c and d,

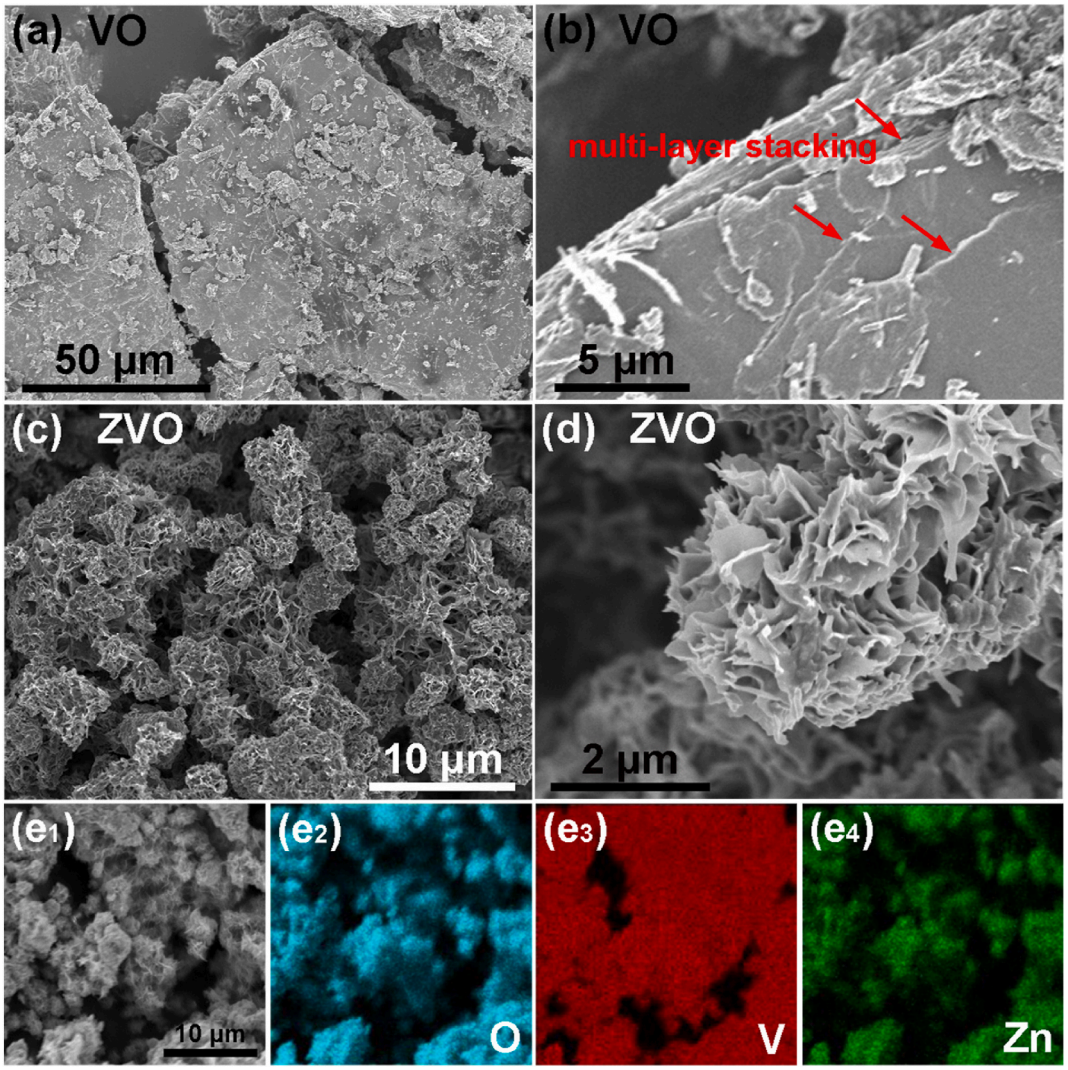

Fig. 2. SEM images of (a,b) VO and (c,d) ZVO powders. (e_1) SEM image of ZVO powder and the corresponding EDS elemental images of (e_2) O, (e_3) V, and (e_4) Zn.

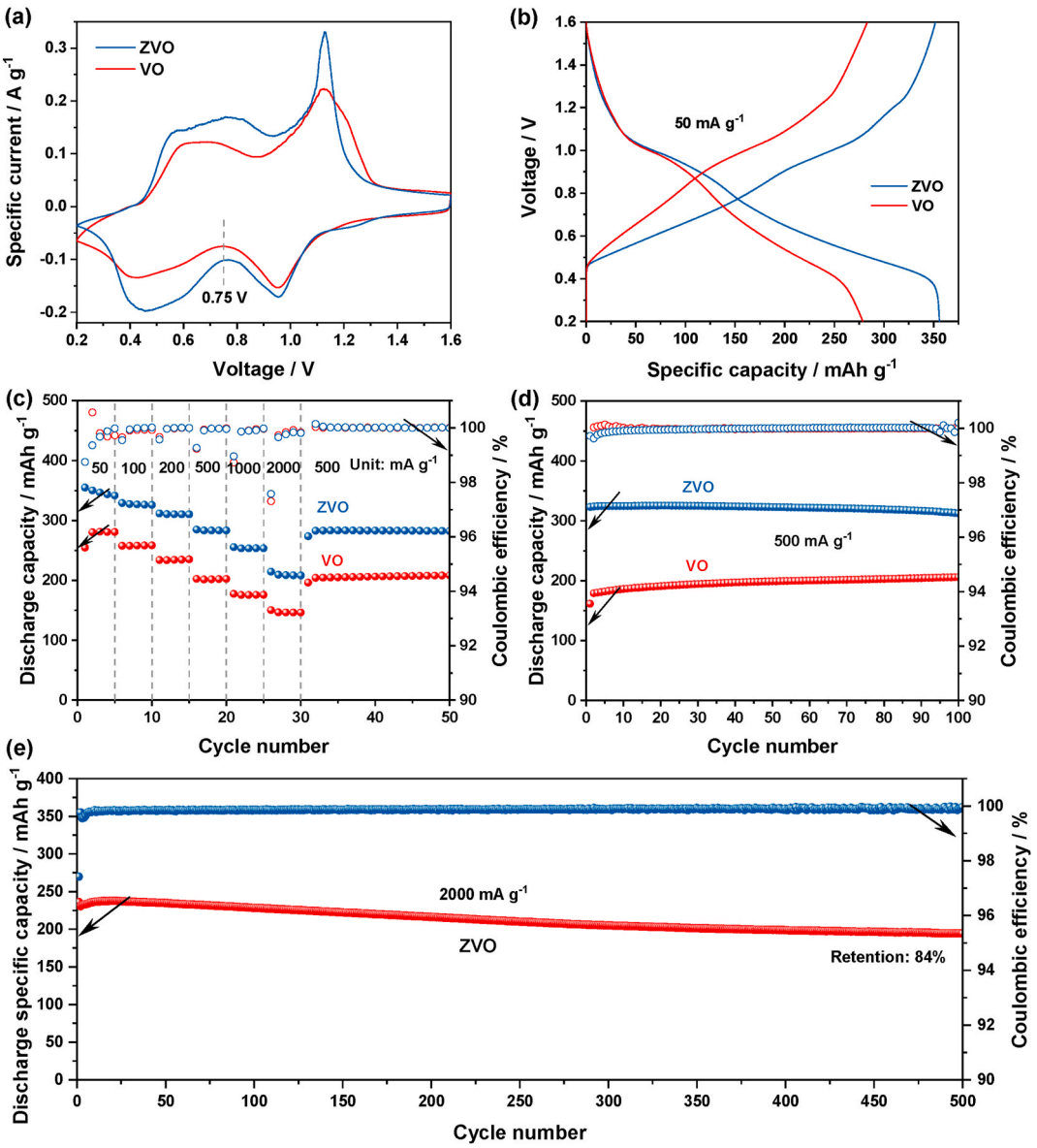

Fig. 3. Electrochemical performance of AZMBs employing VO or ZVO as the cathode material, respectively. (a) CV curves obtained as a scan rate of 0.1 mV s^{-1}. (b) Dis-/charge profiles at 50 mA g^{-1}. (c) Discharge specific capacity and Coulombic efficiency upon the dis-/charge tests at various current rates. Dis-/charge cyclability tested at (d) 500 mA g^{-1} and (e) 2000 mA g^{-1}.

respectively.

During discharge, the pH evolution can be divided in two regions based on the different trends. Above 0.7 V, i.e., **region 1**, the discharge leads to sharp increase of pH, which proves the occurrence of H^+ intercalation. In contrast, the pH value becomes stable, even slight decreasing, upon further discharge below 0.7 V, i.e., **region 2** in Fig. 4c. The cell still delivers a considerable specific capacity in region 2 (Fig. 3b), implying the intercalation of Zn^{2+}. In addition, a short pH plateau is observed for ZVO (**region 3**) only, indicating for an additional Zn^{2+} intercalation step.

The overall pH evolution profiles during charge can be divided to three regions, i.e., **regions 4–6**, as marked in Fig. 4d. In region 4, the pH value is rather flat, resulting from a sudden cell polarization from 0.2 V to around 0.47 V, as displayed in Fig. 3b. Thus, the plateau in **region 4** does not indicate Zn^{2+} de-intercalation. In the following two regions, a decreasing trend of pH is observed, which indicates H^+ de-intercalation. However, the pH decrease is much faster in **region 6** than **region 5**. It should be noted that the pH value is a logarithmic function of the H^+ concentration, so H^+ de-intercalation mainly occurs in **region 6**. Correlating the relatively flat pH evolution in the low voltage **region 2** during discharge and the relatively slower pH decrease in the voltage **region 5** during charge, one can infer that Zn^{2+} de-intercalation mainly occurs in **region 5**. In addition to these, a pH plateau is observed from the profile of ZVO in **region 7**, which indicates de-intercalation of Zn^{2+} and is correlated to **region 3** marked in Fig. 5c. Nonetheless, the capacity of this region is rather limited.

In general, these results show that the de-/intercalation of H^+ and Zn^{2+} mainly occurs in the high voltage and low voltage regions, respectively. Specifically, H^+ and Zn^{2+} intercalation upon discharge mainly occurs in the voltage regions above and below 0.7 V upon, respectively. H^+ and Zn^{2+} de-intercalation upon charge mainly occurs in the voltage region above and below 0.95 V, respectively. These results match well with the two pairs of broad redox peaks in the CV curve (Fig. 3a). Since the specific capacity enhancement through the pre-intercalation strategy mainly comes from the low voltage region as observed from Fig. 3a, one can further infer that such an enhancement is mainly contributed by Zn^{2+} intercalation. Moreover, the results of the *operando* pH tests promote the understanding of the phenomenon

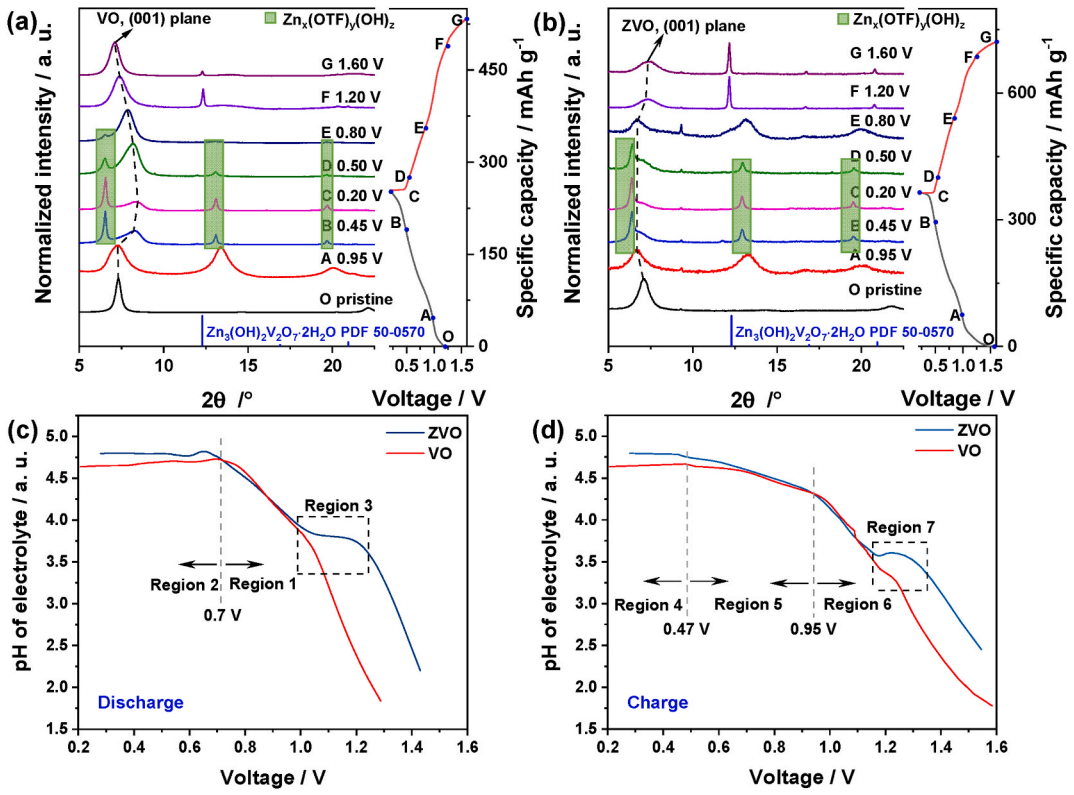

Fig. 4. Ex-situ XRD of (a) VO and (b) ZVO electrodes in the initial discharge and charge cycle. *Operando* pH measurement of electrolytes in close proximity to VO and ZVO electrodes in the initial (c) discharge and (d) charge of the AZMBs at 50 mA g^{-1}.

observed in the *ex-situ* XRD patterns. The appearance of reflections for vanadium-free basic zinc salt (e.g., $Zn_x(OTF)_y(OH)_z$), which is considered to be an indicator of H^+ intercalation [20,21], is observed in the low voltage region (≤0.5 V). However, the *operando* pH measurement indicates that H^+ intercalation already occurs in the beginning of discharge, mainly in **region 1**, i.e., above 0.7 V. This demonstrates that the *operando* pH measurement is more sensitive than XRD detection of $Zn_x(OTF)_y(OH)_z$ as indicator of H^+ intercalation.

In a further step, galvanostatic intermittent titration technique (GITT) was performed on three-electrode AZMBs employing an additional zinc foil as the reference electrode. The potential evolution upon the test is summarized in Fig. 5a. For each titration step, the cell was initially subjected to a constant current (50 mA g^{-1}) pulse for 3 h (τ) followed by an open-circuit stand for 8 h to allow the electrode potential to reach its quasi-steady-state value (E_S). Fig. 5b displays a typical potential evolution for a single titration step. On the basis of this test, the chemical diffusion coefficient (D) of the guest ions can be calculated by the following equation [34]:

$$D = \frac{4}{\pi\tau}\left(\frac{m_B V_M}{M_B S}\right)^2 \left(\frac{\Delta E_S}{\Delta E_\tau}\right)^2$$

where V_M is the molar volume of the active material, M_B and m_B are the molecular weight and the mass of the active material, S is the active surface area of electrode, τ is the duration of the current flux in one titration. ΔE_S and ΔE_τ are the potential change schematically labeled in Fig. 5b. Therefore, for the test of an electrode, the diffusion coefficient of the guest ion is proportional to the $\left(\frac{\Delta E_S}{\Delta E_\tau}\right)^2$ as described in the following equation:

$$D \propto \left(\frac{\Delta E_S}{\Delta E_\tau}\right)^2$$

The calculated $\left(\frac{\Delta E_S}{\Delta E_\tau}\right)^2$ of each titration upon discharge and charge is shown in Fig. 5c and d, respectively. For the discharge process, ZVO exhibits higher values than VO, indicating the promoted intercalation kinetics, which can be attributed to the increased interlayer spacing as evidenced via XRD (Fig. 1a). The additional contribution from the smaller particle size of ZVO with respect to VO (Fig. 2a–d) is expected to be limited due to their very similar specific surface area (Fig. 1d). It is also observed that the $\left(\frac{\Delta E_S}{\Delta E_\tau}\right)^2$ value is higher at higher voltages than at lower voltages, demonstrating that H^+ has faster intercalation kinetics than Zn^{2+} for both the materials in the electrolyte. This means that the intercalation of Zn^{2+} is the step limiting the capacity delivered by the materials, which explains why Zn^{2+} intercalation contributes more to the enhanced specific capacity than that of H^+. For the charge process, ZVO exhibits higher value of $\left(\frac{\Delta E_S}{\Delta E_\tau}\right)^2$ in the low voltage region but comparable value in the high voltage region with respect to VO. This generally fits with the promoted de-intercalation of Zn^{2+} and consequently higher specific capacity in the low voltage region.

3. Conclusions

Zn^{2+} pre-intercalated and neat bilayered V_2O_5 materials were synthesized via a simple and fast microwave-assisted hydrothermal method. The pre-intercalation of Zn^{2+} into bilayered V_2O_5 effectively increased the interlayer distance and the specific capacity in a wide current rate range. The de-/intercalation of H^+ and Zn^{2+} mainly occurs in the high voltage and low voltage regions, respectively. Benefiting from the enlarged interlayer spacing, the intercalation kinetics of both H^+ and Zn^{2+} is promoted. Nonetheless, Zn^{2+} intercalation, being the limiting step for the specific capacity, contributes more than H^+ intercalation to the capacity enhancement of ZVO. Overall, the results presented in this

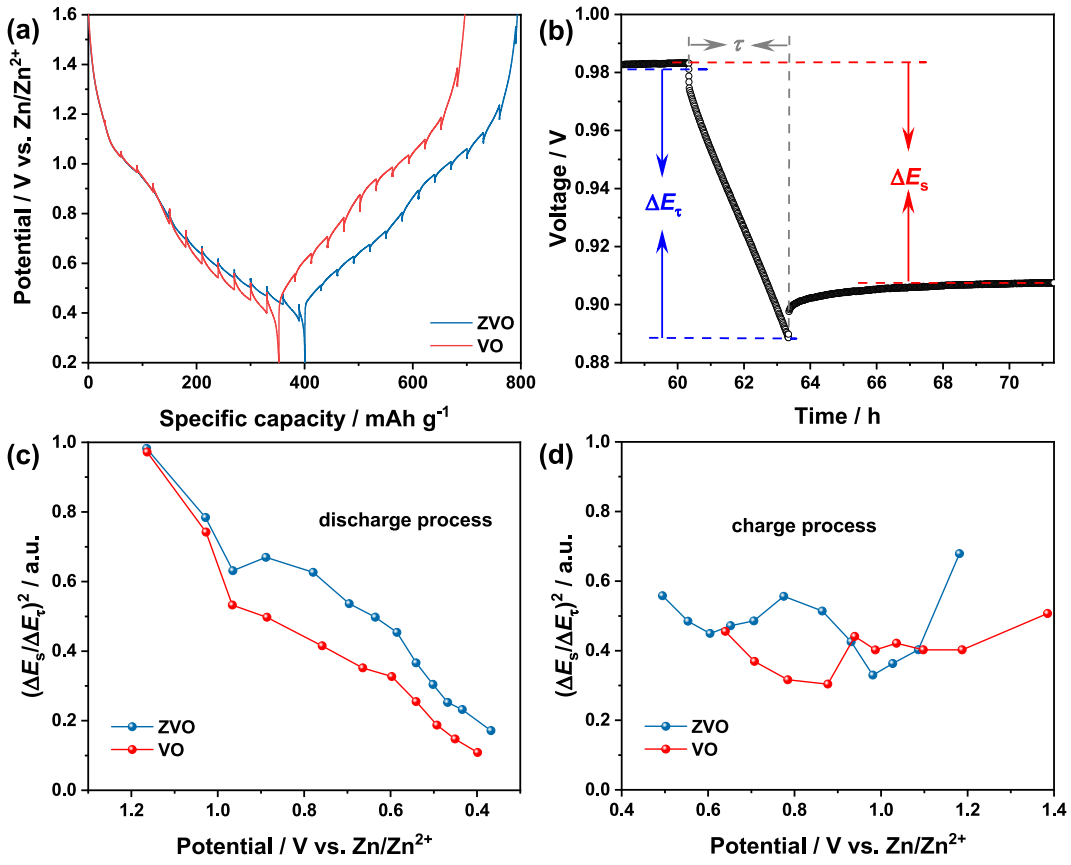

Fig. 5. *GITT tests of VO and ZVO electrodes. (a) Potential evolution upon the test. (b) Typical potential evolution upon a titration step. Calculated* $\left(\frac{\Delta E_s}{\Delta E_\tau}\right)^2$ *of each titration step upon (c) discharge and (d) charge.*

work demonstrate that ZVO is a promising cathode material for high-performance AZMBs and *operando* pH measurements is an effective characterization method allowing, in combination with more conventional techniques, to reveal the complex intercalation chemistry in AZMBs.

4. Experimental section

4.1. Materials

Crystaline V_2O_5 (Pechiney), $Zn(NO_3)_2{\cdot}6H_2O$ (Alfa Aesar), N-methyl-2-pyrrolidone (NMP, anhydrous, Sigma Aldrich), H_2O_2 solution (Sigma Aldrich, 30 wt%), polyvinylidene fluoride (PVdF, Solef 6020), carbon black (Super C65, IMERYS), stainless steel foil (thickness: 50 μm, Goodfellow), zinc foil (thickness: 25 μm, Goodfellow), carbon paper (TP-030T, Quintech), glass fiber sheet (Whatman GF/F), and $Zn(OTF)_2$ (99.5 %, 50 ppm water, Solvionic) were used as received.

4.2. Preparation of VO and ZVO via microwave-assisted hydrothermal method

For the preparation of ZVO, 1 mmol $Zn(NO_3)_2{\cdot}6H_2O$ (297 mg) was dissolved in a mixture of 1.75 mL H_2O_2 aqueous solution (30 wt%) and 19 mL water, which was cooled with ice-water bath. 2.75 mmol crystalline V_2O_5 (500 mg) was then added to the mixture under magnetic stirring. After 1 h, the ice-water bath was removed and the mixture was magnetic stirred at room temperature for another 1 h. Subsequently, the obtained transparent, orange solution was transferred into a glass reactor (30 mL, Anton Paar). The reactor was heated in a microwave oven (Monowave 300, Anton Paar) up to 180 °C in 5 min, and held at this temperature for 30 min with a stirring rate of 300 rpm. The obtained product was thoroughly washed with water and acetone alternatively. After being dried in an oven at 80 °C overnight, ZVO was obtained. VO was prepared following the same procedure without the addition of $Zn(NO_3)_2{\cdot}6H_2O$.

4.3. Physical characterization

XRD was conducted using a Bruker D8 Advance diffractometer (Bruker, Germany) with Cu-Kα radiation in the 2θ range from 5° to 50° while the step length and time for every step were 0.0205° and 6 s, respectively. For *ex-situ* XRD, the 2θ range and step time were changed to 6–25° and 1 s, respectively. The electrodes for the *ex-situ* XRD were taken from the coin cells, which were disassembled in ambient atmosphere. The obtained electrodes were immersed in 5 mL ultrapure water and further flushed with 1 mL ultrapure water. After drying at 80 °C, the electrodes were ready for ex-situ XRD test. The nitrogen adsorption isotherm was measured at 77.3 K using the Autosorb-iQ from Quantachrome. Prior to the measurement, the sample was degassed at 120 °C for 24 h under vacuum. SEM of as-prepared sample was performed on a Zeiss LEO 1550 microscope, equipped with an EDS (Oxford Instruments X-MaxN, 50 mm^2, 15 kV). ICP-OES analysis was carried out on a Spectro Arcos spectrometer (Spectro Analytical Instruments).

4.4. Electrochemical measurements

The cathode electrodes were prepared by doctor-blade casting slurries with 70 wt% active materials (VO or ZVO), 20 wt% C65, and 10 wt% PVdF on stainless steel or carbon paper substrate (carbon paper was used only when the electrodes were prepared for the *operando* pH tests). NMP

was used as the solvent to prepare the slurry. After being dried at 60 °C, electrodes with a diameter of 14 mm or 12 mm were punched and further dried at 120 °C under high vacuum to fully remove the NMP. The average mass loading of the active material was around 3 mg cm^{-2}.

For coin cell type AZMBs, zinc foil disc with a diameter of 16 mm, GF/F glass fiber disc with a diameter of 16 mm, and 100 μL 3 m Zn $(OTF)_2$ aqueous solutions were used as the counter electrode, separator, electrolyte, respectively. For three-electrode Swagelok type AZMBs, zinc foil discs with a diameter of 12 mm and around 2 mm were used as the counter and reference electrodes, respectively. GF/F membrane discs and 100 μL 3 m $Zn(OTF)_2$ aqueous solutions were used as separators and electrolytes, respectively. The cells were kept in open circuit for 3 h before electrochemical tests. The OCV of the "just-assembled" AZMBs employing VO and ZVO as cathodes was around 1.50 and 1.35 V, respectively. After 3 h, the OCV decreased to around 1.49 and 1.24 V, respectively. The *operando* pH measurement was conducted with a designed three-electrode Swagelok type cell employing a pH electrode with a flat membrane detector (Blue line 27 pH, WTW-pH surface measurement with SenTix® Sur). The configuration of the cell and the validation of this *operando* pH measurement were reported in a previously published manuscript by our group [22]. The special design of this cell allows the use of a low amount of electrolyte (only 100 μL per cell) and to measure the pH variation of the electrolyte in close proximity to the working electrode.

A Maccor 4000 Battery system was used for the galvanostatic charge/discharge tests. CV tests were carried out with a galvanostat/potentiostat (VMP3 Bio-Logic, France). GITT was performed with the Maccor 4000 Battery system on three electrodes Swagelok type AZMBs (50 mA g^{-1} for 3 h followed by an 8 h rest). The temperature of the cells for the above tests was controlled to be 20 °C with Binder ovens. For *operando* pH measurements at room temperature (20 ± 2 °C), the charge/discharge of the cells was controlled via a galvanostat/potentiostat VMP (Bio-Logic, France) while the pH values were recorded every 5 min via a pH meter (Lab 860, SI Analytics).

CRediT authorship contribution statement

Xu Liu: Writing – review & editing, Writing – original draft, Investigation, Conceptualization. **Xu Dong:** Writing – review & editing, Writing – original draft, Supervision, Investigation. **Stefano Passerini:** Writing – review & editing, Validation, Supervision, Resources, Project administration, Funding acquisition, Conceptualization.

Declaration of competing interest

The authors declare that they have no known competing financial interests or personal relationships that could have appeared to influence the work reported in this paper.

Data availability

Data will be made available on request.

Acknowledgements

Financial support from the Helmholtz Association is acknowledged.

Appendix A. Supplementary data

Supplementary data to this article can be found online at https://doi.org/10.1016/j.jpowsour.2024.235401.

References

[1] X. Zeng, M. Li, D. Abd El-Hady, W. Alshitari, A.S. Al-Bogami, J. Lu, K. Amine, Commercialization of lithium battery technologies for electric vehicles, Adv. Energy Mater. 9 (2019), https://doi.org/10.1002/aenm.201900161.
[2] A.A. Kebede, T. Kalogiannis, J. Van Mierlo, M. Berecibar, A comprehensive review of stationary energy storage devices for large scale renewable energy sources grid integration, Renew. Sustain. Energy Rev. 159 (2022) 112213, https://doi.org/10.1016/j.rser.2022.112213.
[3] H. Zhang, X. Liu, H. Li, I. Hasa, S. Passerini, Challenges and strategies for high-energy aqueous electrolyte rechargeable batteries, Angew. Chem. Int. Ed. 60 (2021) 598–616, https://doi.org/10.1002/anie.202004433.
[4] S. Wang, Y. Ying, S. Chen, H. Wang, K.K.K. Cheung, C. Peng, H. Huang, L. Ma, J. A. Zapien, Highly reversible zinc metal anode enabled by zinc fluoroborate salt-based hydrous organic electrolyte, Energy Storage Mater. 63 (2023) 102971, https://doi.org/10.1016/j.ensm.2023.102971.
[5] M. Peng, X. Tang, K. Xiao, T. Hu, K. Yuan, Y. Chen, Polycation-regulated electrolyte and interfacial electric fields for stable zinc metal batteries, Angew. Chem. Int. Ed. 62 (2023) e202302701, https://doi.org/10.1002/anie.202302701.
[6] X. Geng, X. Hou, X. He, H.J. Fan, Challenges and strategies on interphasial regulation for aqueous rechargeable batteries, Adv. Energy Mater. 14 (2024) 2304094, https://doi.org/10.1002/aenm.202304094.
[7] Y. Liang, M. Qiu, P. Sun, W. Mai, Comprehensive review of electrolyte modification strategies for stabilizing Zn metal anodes, Adv. Funct. Mater. 33 (2023) 2304878, https://doi.org/10.1002/adfm.202304878.
[8] C. Nie, G. Wang, D. Wang, M. Wang, X. Gao, Z. Bai, N. Wang, J. Yang, Z. Xing, S. Dou, Recent progress on Zn anodes for advanced aqueous zinc-ion batteries, Adv. Energy Mater. 13 (2023) 2300606, https://doi.org/10.1002/aenm.202300606.
[9] Y. Bai, Y. Qin, J. Hao, H. Zhang, C.M. Li, Advances and perspectives of ion-intercalated vanadium oxide cathodes for high-performance aqueous zinc ion battery, Adv. Funct. Mater. 34 (2024) 2310393, https://doi.org/10.1002/adfm.202310393.
[10] C. Xianhong, R. Pengchao, W. Xianwen, L. Shuquan, Z. Jiang, Crystal structures, reaction mechanisms, and optimization strategies of MnO2 cathode for aqueous rechargeable zinc batteries, Chin. J. Inorg. Chem. 38 (2022) 2111003, https://doi.org/10.3866/PKU.WHXB202111003.
[11] J. Liu, Z. Shen, C.Z. Lu, Research progress of Prussian blue and its analogues for cathodes of aqueous zinc ion batteries, J. Mater. Chem. A 12 (2024) 2647–2672, https://doi.org/10.1039/d3ta06641j.
[12] Y.L. Can Jin, Qiuyu Shen, Long Zhang, Shengwei Li, Xuanhui Qu, Lifang Jiao, Advanced polyanionic cathode materials for aqueous zinc-ion batteries: from crystal structures, reaction mechanisms, design strategies to future perspectives, J. Mater. Chem. A 12 (2024) 12926–12944, https://doi.org/10.1039/D4TA01290A.
[13] Z. Bai, G. Wang, H. Liu, Y. Lou, N. Wang, H.K. Liu, S. Dou, Advancements in aqueous zinc-iodine batteries: a review, Chem. Sci. 15 (2024) 3071–3092, https://doi.org/10.1039/d3sc06150g.
[14] X. Wang, L. Liu, Z. Hu, C. Peng, C. Han, W. Li, High energy density aqueous zinc–chalcogen (S, Se, Te) batteries: recent progress, challenges, and perspective, Adv. Energy Mater. 13 (2023) 2302927, https://doi.org/10.1002/aenm.202302927.
[15] J. Ding, H. Gao, D. Ji, K. Zhao, S. Wang, F. Cheng, Vanadium-based cathodes for aqueous zinc-ion batteries: from crystal structures, diffusion channels to storage mechanisms, J. Mater. Chem. A 9 (2021) 5258–5275, https://doi.org/10.1039/d0ta10336e.
[16] Y. Yang, Y. Tang, S. Liang, Z. Wu, G. Fang, X. Cao, C. Wang, T. Lin, A. Pan, J. Zhou, Transition metal ion-preintercalated V2O5 as high-performance aqueous zinc-ion battery cathode with broad temperature adaptability, Nano Energy 61 (2019) 617–625, https://doi.org/10.1016/j.nanoen.2019.05.005.
[17] J. Huang, J. Zhou, S. Liang, Guest pre-intercalation strategy to boost the electrochemical performance of aqueous zinc-ion battery cathodes, Wuli Huaxue Xuebao/Acta Phys. - Chim. Sin. 37 (2021) 2005020, https://doi.org/10.3866/PKU.WHXB202005020.
[18] T. Zhou, G. Gao, Pre-intercalation strategy in vanadium oxides cathodes for aqueous zinc ion batteries: review and prospects, J. Energy Storage 84 (2024) 110808, https://doi.org/10.1016/j.est.2024.110808.
[19] C. Liu, Z. Neale, J. Zheng, X. Jia, J. Huang, M. Yan, M. Tian, M. Wang, J. Yang, G. Cao, Expanded hydrated vanadate for high-performance aqueous zinc-ion batteries, Energy Environ. Sci. 12 (2019) 2273–2285, https://doi.org/10.1039/c9ee00956f.
[20] W. Liu, L. Dong, B. Jiang, Y. Huang, X. Wang, C. Xu, Z. Kang, J. Mou, F. Kang, Layered vanadium oxides with proton and zinc ion insertion for zinc ion batteries, Electrochim. Acta 320 (2019) 134565, https://doi.org/10.1016/j.electacta.2019.134565.
[21] Z. Li, S. Ganapathy, Y. Xu, Z. Zhou, M. Sarilar, M. Wagemaker, Mechanistic insight into the electrochemical performance of Zn/VO2 batteries with an aqueous ZnSO4 electrolyte, Adv. Energy Mater. 9 (2019) 1900237, https://doi.org/10.1002/aenm.201900237.
[22] X. Liu, H. Euchner, M. Zarrabeitia, X. Gao, G.A. Elia, A. Groß, S. Passerini, Operando pH measurements decipher H+/Zn2+intercalation chemistry in high-performance aqueous Zn/δ-V2O5batteries, ACS Energy Lett. 5 (2020) 2979–2986, https://doi.org/10.1021/acsenergylett.0c01767.
[23] A. Moretti, F. Maroni, I. Osada, F. Nobili, S. Passerini, V2O5 aerogel as a versatile cathode material for lithium and sodium batteries, Chemelectrochem 2 (2015) 529–537, https://doi.org/10.1002/celc.201402394.

[24] A. Moretti, S. Passerini, Bilayered nanostructured V2O5·nH2O for metal batteries, Adv. Energy Mater. 6 (2016) 1600868, https://doi.org/10.1002/aenm.201600868.
[25] A. Moretti, G. Giuli, A. Trapananti, S. Passerini, Electrochemical and structural investigation of transition metal doped V2O5 sono-aerogel cathodes for lithium metal batteries, Solid State Ionics 319 (2018) 46–52, https://doi.org/10.1016/j.ssi.2018.01.040.
[26] M. Giorgetti, S. Passerini, M. Berrettoni, W.H. Smyrl, XAS investigation on polyvalent cation intercalation in V2O5 aerogels, J. Synchrotron Radiat. 6 (1999) 743–745, https://doi.org/10.1107/S0909049598015970.
[27] E. Frabetti, G.A. Deluga, M. Giorgetti, M. Berrettoni, W.H. Smyrl, X-Ray absorption spectroscopy study of CuVO and ZnVO aerogel-like cathodes for lithium batteries for lithium batteries, J. Phys. Chem. B 108 (2004) 3765, https://doi.org/10.1021/jp037656.
[28] M. Giorgetti, M. Berrettoni, W.H. Smyrl, Doped V2O5-based cathode materials: where does the doping metal go? An X-ray absorption spectroscopy study, Chem. Mater. 19 (2007) 5991–6000, https://doi.org/10.1021/cm701910c.
[29] P. Aldebert, N. Baffier, N. Gharbi, J. Livage, Layered structure of vanadium pentoxide gels, Mater. Res. Bull. 16 (1981) 669–676, https://doi.org/10.1016/0025-5408(81)90266-X.
[30] Z.A. Alothman, A review: fundamental aspects of silicate mesoporous materials, Materials 5 (2012) 2874–2902, https://doi.org/10.3390/ma5122874.
[31] Q. Wei, Z. Jiang, S. Tan, Q. Li, L. Huang, M. Yan, L. Zhou, Q. An, L. Mai, Lattice breathing inhibited layered vanadium oxide ultrathin nanobelts for enhanced sodium storage, ACS Appl. Mater. Interfaces 7 (2015) 18211–18217, https://doi.org/10.1021/acsami.5b06154.
[32] X. Liu, B. Qin, H. Zhang, A. Moretti, S. Passerini, Glyme-based electrolyte for Na/bilayered-V2O5 batteries, ACS Appl. Energy Mater. 2 (2019) 2786–2793, https://doi.org/10.1021/acsaem.9b00128.
[33] Z. Xing, G. Xu, X. Xie, M. Chen, B. Lu, J. Zhou, S. Liang, Highly reversible zinc-ion battery enabled by suppressing vanadium dissolution through inorganic Zn2+ conductor electrolyte, Nano Energy 90 (2021) 106621, https://doi.org/10.1016/j.nanoen.2021.106621.
[34] Z. Li, F. Du, X. Bie, D. Zhang, Y. Cai, X. Cui, C. Wang, G. Chen, Y. Wei, Electrochemical kinetics of the Li[Li0.23Co0.3Mn 0.47]O2 cathode material studied by GITT and EIS, J. Phys. Chem. C 114 (2010) 22751–22757, https://doi.org/10.1021/jp1088788.